Transport in Porous Media (2021) 137:215–232
https://doi.org/10.1007/s11242-021-01559-5

Speeding-up Simulation of Multiphase Flow in Digital Images of Heterogeneous Porous Media by Curvelet Transformation

Abdullah Aljasmi[1] · **Muhammad Sahimi**[1]

Received: 28 September 2020 / Accepted: 28 January 2021 / Published online: 18 February 2021

Abstract
Multiphase fluid flow in porous media is important to a wide variety of processes of fundamental scientific and practical importance. Developing a model for the pore space of porous media represents the first step for simulating such flows. With rapid increase in the computation power and advances in instrumentation and imaging processes, it has become feasible to carry out simulation of multiphase flow in two- and three-dimensional images of porous media, hence dispensing with development of models of pore space that are based on approximating their morphology. Image-based simulations are, however, very time consuming. We describe an approach for speeding-up image-based simulation of multiphase flow in porous media based on curvelet transformations, which are specifically designed for processing of images that contain complex curved surfaces. Most porous media contain correlations in their morphology and, therefore, their images carry redundant information that, in the curvelet transform space, can be removed efficiently and accurately in order to obtain a coarser image with which the computations are far less intensive. We utilize the methodology to simulate two-phase flow of oil and water in two-dimensional digital images of sandstone and carbonate samples, and demonstrate that while the results with the curvelet-processed images are as accurate as those with the original ones, the computations are speeded up by a factor of 110–150. Thus, the methodology opens the way toward achieving the ultimate goal of simulation of multiphase flow in porous media, namely, making image-based computations a standard practice.

Keywords Two-phase fluid flow · Porous media · Curvelet transformation

1 Introduction

Multiphase flow in heterogeneous porous media is important to many fundamental scientific problems, as well as industrial applications (Helmig and Schulz 1997; Sahimi 2011; Blunt 2017). Examples include evaporation and drying in soil (Shokri et al. 2009,

✉ Muhammad Sahimi
moe@usc.edu

[1] Mork Family Department of Chemical Engineering and Materials Science, University of Southern California, Los Angeles, California 90089-1211, USA

2010, 2012; Shokri 2014; Shokri-Kuehni et al. 2017a, b, 2018), ink imbibition in printing paper (Ghassemzadeh et al. 2001; Ghassemzadeh and Sahimi 2004; Swerin 2018; Aslannejad and Hassanizadeh 2017; Aslannejad et al. 2019), extraction of oil, gas and geothermal energy from porous formations, transport of contaminants in soils and aquifers, and sequestration of CO_2 in depleted oil reservoirs (Friedlingstein and Solomon 2005; Nordbotten and Celia 2011; Kohanpur et al. 2020). Aside from the classical continuum models of such phenomena (Bear 1972), studies of multiphase flows in a porous medium entail, as the first step, developing models of its pore space. There is a wide variety of such models in the literature, ranging from percolation models (for a recent review see Hunt and Sahimi 2017), both random (Larson et al. 1977; Heiba et al. 1992; Sahimi et al. 1986; Kantzas and Chatzis 1988; Blunt and Scher 1995) and invasion percolation (Chandler et al. 1982; Wilkinson and Willimsen 1983; Knackstedt et al. 2001 for a simple introduction to invasion percolation see Ebrahimi 2010), detailed pore-network models (Blunt and King 1991; Blunt et al. 1992; Blunt 1997; Piri and Blunt 2005a, b), and a combination of effective-medium approximation and percolation theory (Ghanbarian et al. 2016). Although such models have provided much insight into the physics of multiphase flow in porous media, the way the morphology of the pore space, i.e., its pore-size distribution, pore connectivity, and the pore shape, is represented is based on assumptions, approximations, and sometimes even unreasonable simplifications.

Two- and three-dimensional (3D) images of porous media have been becoming important tools for their characterization because, depending on their resolution, such images provide detailed information about the morphology of the pore space. With advances in instrumentation, acquisition of high-resolution 2D and 3D images by focused ion-beam scanning electron microscopes (Lemmens et al. 2011), magnetic resonance imaging (Sheppard et al. 2003; Sankey et al. 2009) and X-ray computed tomography (Arns et al. 2001, 2002; Porter et al. 2010; Iglauer et al. 2010; Berg et al. 2013; Wildenschild et al. 2014) that can be used to display the fluid distributions in 3D have become an essential part of studying various phenomena in porous media. But, in addition to enabling their precise characterization, high-resolution images of porous media have another advantage: provided that their size is larger than the representative elementary volume (REV), they may be used in direct numerical simulation of fluid flow and transport in the porous media without any need for developing models of their pore space that entails making assumptions and approximations. The REV is the minimum size of a porous medium such that for sizes larger than the REV the medium's properties are independent of its dimensions.

Numerical simulation of the governing equations of fluid flow and transport in the images of porous media is computationally very expensive. Pores in natural and even many synthetic porous media have irregular shapes. Their surface is rough, often representing a self-affine fractal structure. The connectivity of the pores is also complex, giving rise to highly tortuous flow paths. The computational grid that must represent all such complexities faithfully must have high resolution, particularly near the pores' surface. Moreover, a computational grid with equal grid blocks is highly inefficient and increases unnecessarily the computational burden. Use of irregular computational grids with higher resolution segments near the pores' surface and coarser ones away from it is a step in the right direction, but the computations are still highly intensive. Simulation of flow phenomena with the lattice-Boltzmann approach is even slower. For direct image-based simulation of fluid flow and transport in porous media to become the standard approach, particularly when one deals with more than one fluid phase, the speed of the calculation must increase very significantly without losing accuracy.

In this paper, we present a novel approach for image-based simulation of multiphase flow in porous media. Instead of focusing on developing methods that can solve the governing equations more efficiently, we focus on the image itself. We propose a method whereby, taking advantage of extended correlations in the image, we first process it in order to develop a coarser image, and then carry out numerical simulation of two-phase flow in the processed image. The processing of the image is done by curvelet transformations (CTs), a powerful method developed by computer scientists for image processing. We demonstrate that the new method increases the speed of computations by two orders of magnitude or more, while preserving the accuracy of the solution.

The rest of this paper is organized as follows. In the next section, we describe the essential features of CTs that are used in the new methodology. Next, we explain how CTs are used to process the images in order to remove their non-essential features. The porous media and the two-phase flow problem are described next, followed by the presentation of the results. We then discuss a few key aspects of the proposed method. The paper is summarized in the last section.

2 Continuous Curvelet Transformations

Segmentation and processing of an image in order to obtain its sparse but accurate representation has been an active research field, going back many decades. But it was the seminal works of Daubechies (1988, 1992) and Mallat (1989a, b) that advanced the field significantly. They introduced multiresolution wavelet transforms (WTs), a generalization of the Fourier transform, which provide high accuracy in segmenting various types of images, and have been used widely in image processing. The idea is to decompose a 2D image into a series of high- and low-pass filter bands and extract details that characterize horizontal, vertical, and diagonal features through the WTs. If, however, the image is highly noisy and contains curved surfaces, such as images of heterogeneous porous media, the three directions are not enough to capture adequate amount of information in a 2D image. But the WTs have been used very fruitfully in upscaling of geological models of heterogeneous porous media (Mehrabi and Sahimi 1997; Ebrahimi and Sahimi 2002, 2004; Pancaldi et al. 2007; Rasaei and Sahimi 2008, 2009; Babaei and King 2011; Rezapour et al. 2019) and many other applications.

To improve the segmentation, the ridgelet transform, a first-generation CT, was introduced. Its limitation is that it is accurate mostly for detecting linear radial structures, which are not the type that one has in many types of images, ranging from those in medical science (Al-Zubi et al. 2011), to heterogeneous porous media. Thus, the second generation of CTs was introduced (Donoho 1999; Candés et al. 2005, which have been shown to be highly effective at identifying an image's important features along curves, an aspect that is highly important to the rough pores' surface of a porous medium.

The CTs are geometric multiscale transforms that make it possible to have optimal sparse representation of an image with second-order continuous differentiable singularities by precise representation of the edges along curves with very high directional sensitivity. They have already been used in geoscience (Olhede and Walden 2004; Herrmann et al. 2007; Neelamani et al. 2008; Dashtian and Sahimi 2014) for denoising of seismic data. Ma and Plonka (2009) describe other applications. In what follows, we describe CTs for 2D images; its extension to 3D will be discussed later in this paper.

Processing of an image by the CT is carried out in the frequency space. In order to construct a curvelet, two windows are introduced. One of them, $W(r)$, is a radial window with r being the polar coordinate, while the second, $V(\theta)$, represents an angular window. The two functions are smooth and nonnegative, taking on real values and satisfying

$$\sum_{j=-\infty}^{\infty} W^2(2^j r) = 1, \quad r \in (3/4, 3/2) \tag{1}$$

$$\sum_{j=-\infty}^{\infty} V^2(\theta - j) = 1, \quad \theta \in (-1/2, 1/2), \tag{2}$$

with θ being the polar coordinate. The two windows are used to construct a third window U_j in the Fourier space, defined by

$$U_j(r, \theta) = 2^{-3j/4} W(2^{-j} r) V(2^{\lfloor j/2 \rfloor} \theta)/(2\pi), \tag{3}$$

with $[\cdot]$ indicating the number's integer part. By definition, the support of U_j - the domain in which it is nonzero - is a polar wedge defined by $W(r)$ and $V(\theta)$. U_j is applied with scale-dependent window widths in the radial and angular directions. The symmetric version of U_j, $U_j(r, \theta) + U_j(r, \theta + \pi)$, is used in order to ensure that it takes on real values.

Given U_j, the curvelet $\varphi_i(\mathbf{x})$, usually referred to as the mother curvelet, analogous to the mother wavelet for the WTs and referred to as such because all the curvelets at scale 2^{-j} are obtained by rotation and translation of $\varphi_i(\mathbf{x})$, is defined by its Fourier transform,

$$\widehat{\varphi}_i(\boldsymbol{\omega}) = U_j(\boldsymbol{\omega}), \tag{4}$$

where $U_j(\omega_1, \omega_2) = U(\boldsymbol{\omega})$. A sequence of scale-dependent rotation angles, $\theta_l = 2\pi \times 2^{-\lfloor j/2 \rfloor}$ with, $l = 0, \quad 1, \ldots$ and $\theta_l = 0$, and one of translation parameters with $k = (k_1, k_2) \in Z^2$ are introduced. Then, the curvelets as a function of $\mathbf{x} = (x_1, x_2)$ at scale 2^{-j}, orientation θ_l, and position $x_k^{(j,l)} = \mathbf{R}_{\theta_l}^{-1}(k_1 \times 2^{-j}, k_2 \times 2^{-j/2})$ are constructed by (Donoho (1999); Candés et al. (2005))

$$\varphi_{j,l,k}(\mathbf{x}) = \varphi_j\left[\mathbf{R}_{\theta_l}\left(\mathbf{x} - \mathbf{x}_k^{(j,l)}\right)\right], \tag{5}$$

where $\mathbf{R}_{\theta_l}$ represents a rotation by θ_l radians, given by

$$\mathbf{R}_{\theta_l} = \begin{pmatrix} \cos\theta_l & \sin\theta_l \\ -\sin\theta_l & \cos\theta_l \end{pmatrix}, \tag{6}$$

with $\mathbf{R}_{\theta_l}^{-1} = \mathbf{R}_{\theta_l}^{\mathrm{T}} = \mathbf{R}_{-\theta_l}$, and T representing the transpose operation.

We assume that a 2D image of a porous medium, a $n \times n$ array of pixels, is represented by $f(\mathbf{x})$. Then, its CT, usually referred to as the curvelet coefficients (CCs) $C_{j,l,k}$, analogous to wavelet detail coefficients, are defined by

$$C_{j,l,k} = \left\langle f, \varphi_{j,l,k} \right\rangle = \int f(\mathbf{x}) \overline{\varphi_{j,l,k}}(\mathbf{x})\, d\mathbf{x}, \tag{7}$$

with the overline denoting a complex conjugate. Because the CTs are constructed and used in the frequency domain, use of the Plancherel's theorem allows us to rewrite the integral in Eq. (7) in the frequency domain,

$$C_{j,l,k} := \frac{1}{(2\pi)^2}\int \hat{f}(\boldsymbol{\omega})\overline{\widehat{\varphi}_{j,l,k}}(\boldsymbol{\omega})d\boldsymbol{\omega} = \frac{1}{(2\pi)^2}\int \hat{f}(\boldsymbol{\omega})U_j(R_{\theta l}\boldsymbol{\omega})\exp(i\langle \mathbf{x}_k^{j,l},\boldsymbol{\omega}\rangle)d\boldsymbol{\omega}. \quad (8)$$

In addition, a window W_0 is introduced by, $|W_0(r)|^2 + \sum_{j=0} W(2^{-j}r)|^2 = 1$. We define for $(k_1, k_2) \in Z$ the coarse-scale curvelets by, $\varphi_{j_0,k}(\mathbf{x}) = \varphi_{j_0}(\mathbf{x} - 2^{-j_0}\mathbf{k})$ and $\widehat{\varphi}_{j_0}(\boldsymbol{\omega}) = 2^{-j_0}W_0(2^{-j_0}|\boldsymbol{\omega}|)$. This is in complete analogy with the WTs, where coarse-scale wavelet coefficients are also defined, except that the coarse-scale curvelets are nondirectional, i.e., unlike the WTs they are not specific to the three aforementioned directions. Then, the complete CT consists of the fine-scale directional curvelets $(\varphi_{j,l,k})_{j=j_0,l,k}$ and the coarse-scale isotropic $(\Phi_{j_0,k})_k$, which is called the father wavelet.

3 Spatial Correlations and Removal of Redundancy from Images of Porous Media

A common characteristic of the morphology of porous media is extended spatial correlations between the pores and grains. The same correlations exist, of course, in the neighboring pixels (voxels in 3D) of the media's images, and therefore, the image contains redundant information that may be removed. In other words, the foremost task for speeding-up image-based simulation of fluid flow and transport in porous media is perhaps developing a compressed or coarsened representation of the image by removing the redundant information. This is the main idea that we propose in this paper for speeding-up image-based simulation of multiphase flow in porous media: we denoise the image and remove the redundant information, i.e., those features of the morphology that are not essential to fluid flow.

The denoising is based on the fact that (Starck et al. 2002) the CCs represent a measure of the local complexity of an image. In an image of a porous medium the complexity is caused by the pores' rough surface, which is typically a self-affine fractal (see (Sahimi 2011) for a comprehensive discussion) containing the aforementioned correlations and their associated irregular shapes. In other words, the CCs, particularly those associated with the interface between the pores and the solid matrix and their neighborhood, represent a measure of roughness or curviness of the interface. Because of the extended correlations, however, even the pores are affected. Therefore, the larger the CCs, the more significant are the curviness and the roughness. Clearly, if the roughness is severe, its contribution to image-based simulation of two-phase flow is significant. Thus, if we keep only the most curved portions of the pore space and smoothen the rest, a coarser computational grid should suffice for the simulations.

Denoising of images by the WTs was considered the ideal approach, until its aforementioned shortcomings became clear, hence motivating the development of the second generation of the CTs. While there are several ways of exploiting the CTs to denoise or coarsen an image (Starck et al. 2002), we take the simplest approach that, as we demonstrate shortly, suffices for our purpose. The approach represents what is usually referred to as *thresholding*: After curvelet transforming of an image and computing the CCs $C_{j,l,k}$, we normalize them by their largest value. We then introduce a threshold $0 \leq \varepsilon < 1$, such that if $C_{j,l,k} < \varepsilon$, we set it to zero, hence ignoring the local roughness and complexity in that particular neighborhood. We, therefore, obtain a sparser representation of the image in the curvelet space, as many of the CCs of the original image are set to zero. The choice of the numerical value of ε depends on the computation time and resources that one can afford and has access to. We shall return to this point shortly. We then have two options:

(i) We compute the inverse CT of the thresholded image and carry out numerical simulation of two-phase flow in it, or
(ii) the governing flow equations are curvelet transformed and solved in the CT space. Then, the inverse CT of the numerical results is computed numerically. The results presented in this paper were obtained with option (i), but we will also discuss the numerical procedure with (ii).

4 The Porous Media

We utilized 2D images of two distinct types of porous media. One was from a sample of Mt. Simon sandstone (named for Mount Simon escarpment in Eau Claire County, Wisconsin) at a depth of 6700 feet (Tahmasebi et al. 2017; Bakhshian et al. 2018; Kohanpur et al. 2020). The formation is located at verification well number 2 of a study site in Decatur, Illinois, where Illinois State Geological Survey carried out a pilot injection study to better understand the feasibility of full-scale carbon dioxide sequestration by injecting it into the formation. A core plug from the formation was scanned by micro-CT imaging to produce a series of grey-scale scans. We utilized one 2D slice of the image with 512^2 pixels and porosity of 0.25.

The second image, also of size 512^2 pixels, was from a fossiliferous outcrop carbonate, Mt. Gambier limestone in South Australia with porosity of 0.43. We showed previously (r38) that the selected size of both samples exceeds that of a REV. The physical sizes of the images of the sandstone and carbonate rock were, respectively, 1.4 mm^2 and 2.76 mm^2. Figure 1 shows the images.

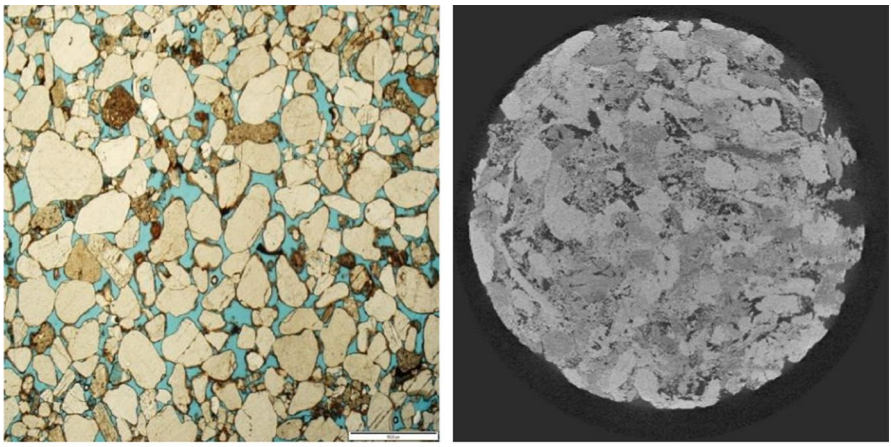

Fig. 1 The images of the two porous media used in the simulations. **a** The Mt. Simon sandstone. **b** Mt. Gambier carbonate

5 The Governing Equations and the Numerical Simulation Procedure

We simulated two-phase flow of water and oil in the images of the two porous media. In both cases, water was injected into the (image) of the pore space, saturated by oil. The contact angle for the water phase was 55°. To carry out the numerical simulations, we used the OpenFOAM program [60], an open-source software that uses finite-volume discretization to solve the continuity and the Stokes' equations in the pore space. The computational grid was unstructured with grid sizes of 2^3 and 1 pixel in the pores and throats, and corner points between the solid boundaries, respectively. Thus, the grid blocks in the throats and the corners were half the size in each direction of those used in the pores. To do so, we used a modified OpenFOAM mesh generator (Ubink 1997; Raeini 2013).

In order to carry out numerical simulations of two-phase flow in porous media, one must upscale the microscopic dynamic and capillary pressures to the Darcy-scale pressure, for which there are various methods. We used the velocity-weighted average of the viscous forces, as well as the velocity-weighted average of the pore-scale pressure gradient that has been shown (Raeini et al. 2014) to produce numerical results that are in agreement with experimental data most closely. The same equations with some modifications can be used to calculate the macroscopic pressure drop in two-phase flow. Thus, the method was used to calculate the total macroscopic pressure drop ΔP_α in the fluid phase α:

$$\Delta P_\alpha = -\frac{1}{Q_\alpha}\int \mathbf{v}\cdot[\boldsymbol{\nabla}\cdot(\mu\boldsymbol{\nabla}\mathbf{v})]dV_\alpha, \quad \alpha = 1,2, \tag{9}$$

where the density ρ and viscosity μ are given by

$$\mu = \phi\mu_1 + (1-\phi)\mu_2, \tag{10}$$

$$\rho = \phi\rho_1 + (1-\phi)\rho_2. \tag{11}$$

Here, Q_α is the flow rate of fluid phase α, $\mathbf{v}$ is the velocity field, V_α is the portion of pore volume filled with phase α, μ_1 and μ_2 are viscosities of the two fluids, and ϕ is the volume fraction of fluid 1 (water) in each grid block. More details are given by Raeini et al. (2014).

The computational grid is Eulerian, for which various methods have been developed in order to include the interfacial tension in it and reduce numerical diffusion at the interface between the two fluids. Such methods include the continuous surface stress (CSS) (Gueyffier et al. 1999), continuous surface force (CSF), sharp surface force (SSF) (Francois et al. 2006), and filtered surface force (FSF) (Raeini et al. 2012). The CSF suffers from spurious velocity in the flow field. The shortcoming is, to some extent, circumvented by the SSF method that controls the sharpness of the capillary pressure by defining a sharpened indicator function, which is the same as the volume fraction ϕ of fluid phase 1. Thus, it takes on a value of one in fluid 1—the wetting fluid—and zero in fluid 2—the non-wetting fluid—and varies smoothly between 0 and 1 in the interface region. A slightly modified indicator function with a capillary force that, relative to the SSF approach, is smoother is used in the FSF approach for the interface motion, which compresses the transition area of the capillary pressure and, hence, resolves the issue with the non-physical velocities that may arise. Then, the capillary pressure transition area is only one grid block. Therefore, we utilized the FSF formulation, since the morphology of the two porous media in which we simulate two-phase flow is complex. The magnitude f of the interfacial force $\mathbf{f}$ is given by

$$f = \kappa\sigma \frac{2\rho}{\rho_w + \rho_{nw}} \nabla\phi, \tag{12}$$

where σ is the interfacial tension, and κ is the curvature given by

$$\kappa = -\nabla \cdot \left(\frac{\nabla\phi}{|\nabla\phi|} \right). \tag{13}$$

The governing equation, in addition to the usual mass conservation, is the momentum equation,

$$\frac{\partial}{\partial t}(\rho \mathbf{v}) = -\nabla P + \nabla \cdot (\mu \nabla \mathbf{v}) + \mathbf{f}. \tag{14}$$

At each time step, the volume fraction ϕ, which indicates the position of the interface between the two-phases, is first updated, followed by the calculation of the interfacial force f. Then, the velocity and pressure fields are computed based on the Stokes' and continuity equations. After the steady-state is reached, the Darcy's law for two-phase flow,

$$\mathbf{v}_\alpha = -\frac{K_{\alpha r} k}{\mu_\alpha} \nabla P_\alpha, \quad \alpha = 1, 2, \tag{15}$$

is used to calculate the relative permeability $K_{\alpha r}$ of fluid phase α as a function of its saturation. As for the fluid properties, we used those given by Oak et al. (1990) who also reported experimental data for the relative permeabilities. They are, $\mu_1 = 1.05 \times 10^{-3}$ for water, $\mu_2 = 1.4 \times 10^{-3}$ for oil, both in Pa.s, and $\rho_1 = \rho_2 = 10^3$ kg/m^3 for the densities. The interfacial tension was $\sigma = 30$ mN/m. Water was injected into the pore space with a velocity of 1.4 cm/s, while the pressure was atmospheric on the opposite face of the injection surface. Thus, the capillary number was $\mathrm{Ca} = 5 \times 10^{-5}$.

6 Results

To compare the results computed with the original images and their coarsened counterparts, we first determined the resolution (number of grid blocks) of the computational grids in the images that yields macroscopic Darcy permeability that no longer changes if the resolution is increased further. Figure 2 presents the results. Thus, we carried out a series of simulations, one with the original image with a computational grid indicated by Fig. 2, and a series of simulations with coarsened images after they had been denoised by the CT.

Figures 3 and 4 compare, respectively, the evolution with time of the water and oil distributions in the original image of the sandstone and carbonate rock with those obtained with the curvelet-thresholded images with the thresholds $\varepsilon = 0.5$, 0.7 and 0.9. The essential features of the distributions are completely similar in all the images. Numerically, the differences between the saturations in the original images and the thresholded ones are less than 5 percent.

To make quantitative comparison between the results obtained with the original images and their thresholded versions, we present in Fig. 5 the water saturation profiles along the macroscopic direction of flow at the breakthrough time t_B, where $X = x/L$, with L being the linear size of the images. The agreement in all cases is excellent.

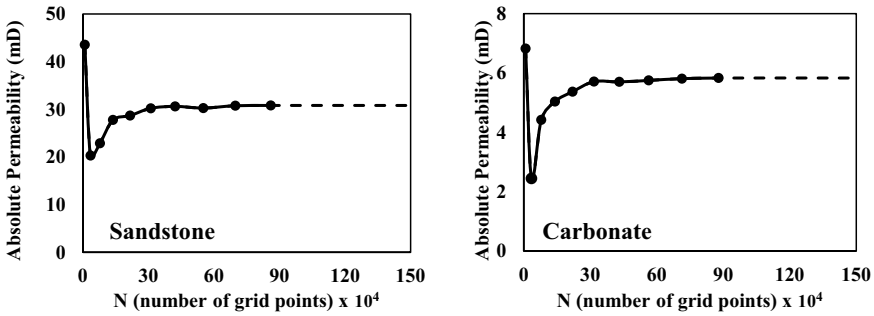

Fig. 2 Dependence of the permeability of the two porous media on the size of the computational grid. **a** The Mt. Simon sandstone. **b** Mt. Gambier carbonate

Figure 6 presents the evolution with the time t_D of the water saturation S_w in the original images of the two porous media and compares it with those computed with the thresholded images, where $t_D = t/t_B$, with t being the actual time. Once again, the agreement is excellent in all the cases.

Figures 7 and 8 compare the distribution of local flow velocities in the two original images with those computed with the thresholded images. The velocities were normalized with respect to their maximum value. For velocities up to the maximum of the distributions, the agreement between all the distributions is perfect. Beyond the maximum, the agreement is good, with all the distributions having the same shape and almost identical tails.

Figures 9 and 10 present the comparison between the relative permeabilities K_r of the two fluid phases, computed in the original images of the two porous media, and those calculated with the thresholded images. The agreement is excellent in all the cases, indicating the accuracy of the computations with the thresholded images.

Finally, an important quantity in two-phase flow in porous media is the oil residual saturation S_{or}, i.e., its saturation at the water breakthrough point. In Table 1, we compare the computed residual saturations in the original images and their thresholded counterparts. In both the sandstone and carbonate porous sample, the maximum difference between the residual saturations in the original image and the thresholded ones with a threshold as high as $\varepsilon = 0.9$ is only 4.5 percent.

7 Discussion

A few important aspects of the results should be discussed in detail.

7.1 Accuracy and Speed-up of the Computations with the Denoised Images

We point out that the computational cost of curvelet transformation of a digitized image of size $n \times n$ is $\mathcal{O}(n^2 \log n)$. But the entire computation time for curve transforming of an image, thresholding it, and obtaining the inverse CT of the coarser image represents only a small fraction of the total computation time for simulating two-phase flow in the image.

In Table 1, we compare the details of the computations: the total number N of grid blocks, the CPU times for all the cases, and the oil residual saturations.

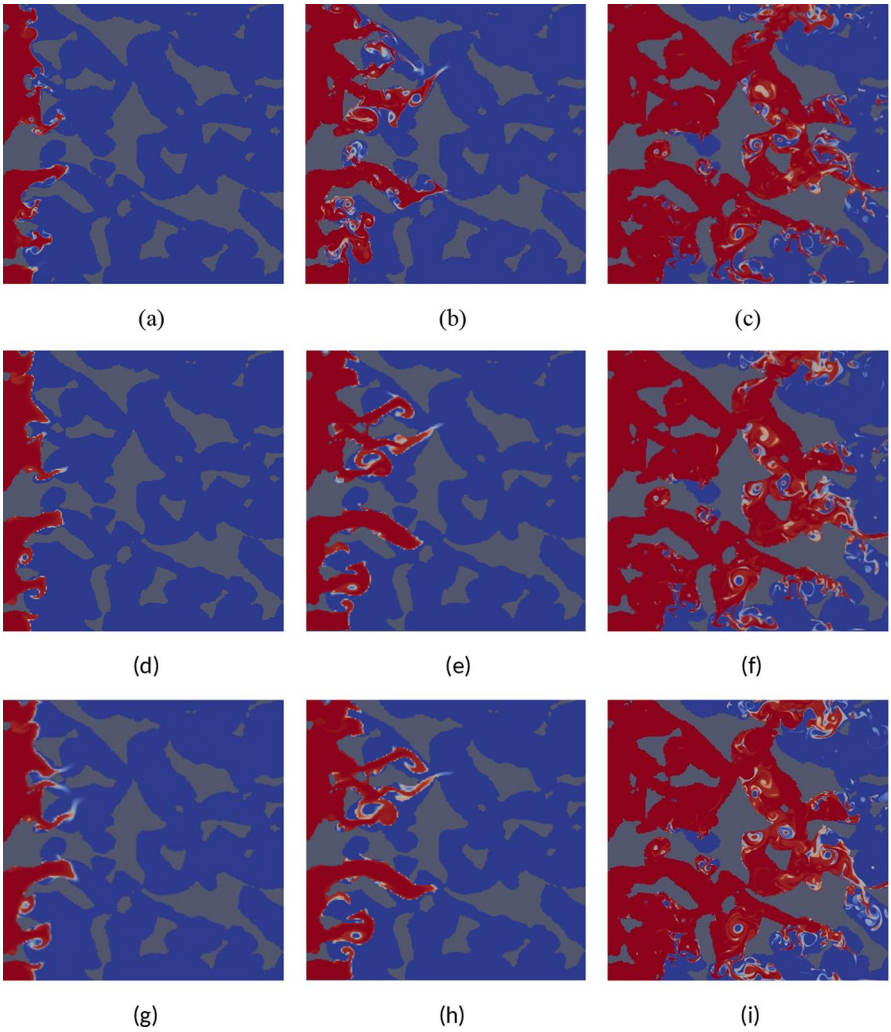

Fig. 3 Evolution of the water distribution (red) and oil (blue) in **a**–**c** the original image of the sandstone; **d**–**f** the thresholded image with a threshold $\epsilon = 0.5$, and **g**–**i** the denoised image with $\epsilon = 0.9$. The times, from left to right, are 30 ms, 60 ms, and at the breakthrough

Two aspects of Table 1 are noteworthy. One is that the computed results with the thresholded images with a threshold as high as $\epsilon = 0.9$ are still very accurate, and differ from those of the original images by less than 5 percent, which is well within the possible inaccuracies that the images themselves may contain. The second aspect is the increase in the speed of the computations for both types of porous media. With a threshold $\epsilon = 0.5$, for which the difference between the computed results with the original and denoised images is about 3.5 percent, the speed-up factor is between 105 and 111, better than two orders of magnitude improvement. When the threshold is increased to 0.9, the speed-up factor is between 144 and 151.

The reason is removal of the redundant and irrelevant information from the images that make it possible to use a coarser but still accurate computational grid. Figure 11 shows the

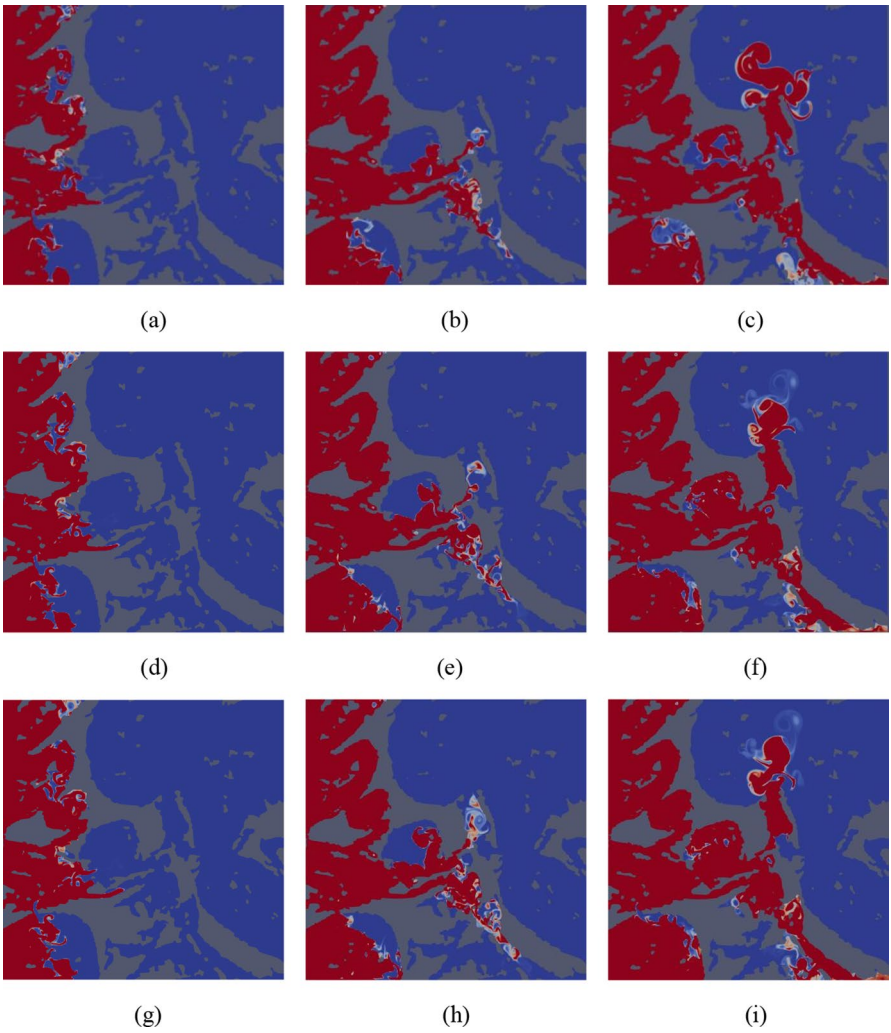

Fig. 4 The same as in Fig. 3, but for the carbonate sample

structure of the grid in a small portion of the original image of the sandstone and compares it with those in two of its coarsened versions. First, note that the grid blocks in Fig. 11a next to the solid walls are highly resolved, because the surface is very complex. Second, after the images are denoised, one no longer needs using a highly resolved computational grid everywhere, but only in selected areas, which are determined by the CT, including portions of the pores since they are correlated with the regions near the solid surface.

7.2 Computations in the Curvelet Space

As already mentioned, one may carry out the simulations in the curvelet space by the following procedure. After the images are curvelet-transformed, no threshold is applied,

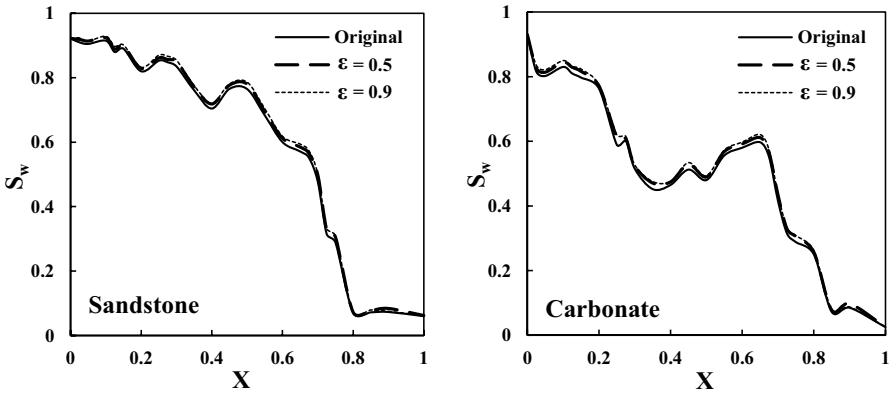

Fig. 5 Saturation profiles of the water phase along the flow direction x at the breakthrough in the curvelet-transformed images of the two porous media, and their comparison with those in the original images. X is the normalized distance of the interface from the inlet, $X = x/L$, where L is the length of the sample in the x direction

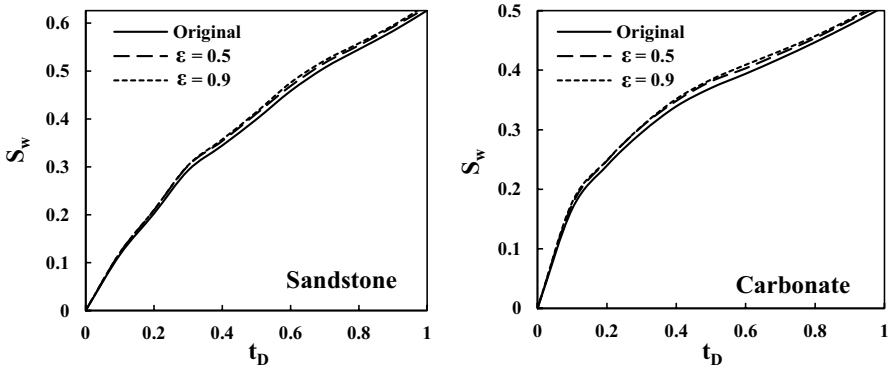

Fig. 6 Evolution of the saturation of the water as a function of the time $t_D = t/t_B$, where t_B is the breakthrough time, in the curvelet-transformed images of the two porous media with two thresholds ϵ and their comparison with those in the original images

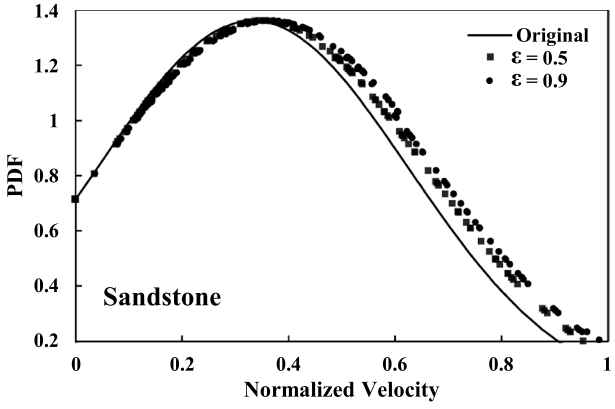

Fig. 7 The probability density function (PDF) of the local (pore) velocity of water, normalized by the maximum flow velocity, in the curvelet-transformed images of the Sandstone with two thresholds ϵ, and their comparison with those in the original image

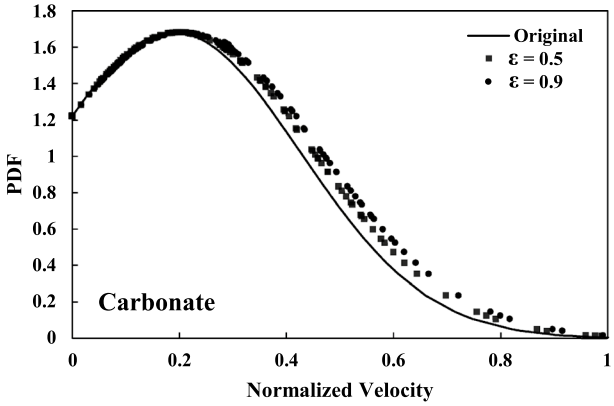

Fig. 8 Same as in Fig. 7, but for the carbonate porous medium

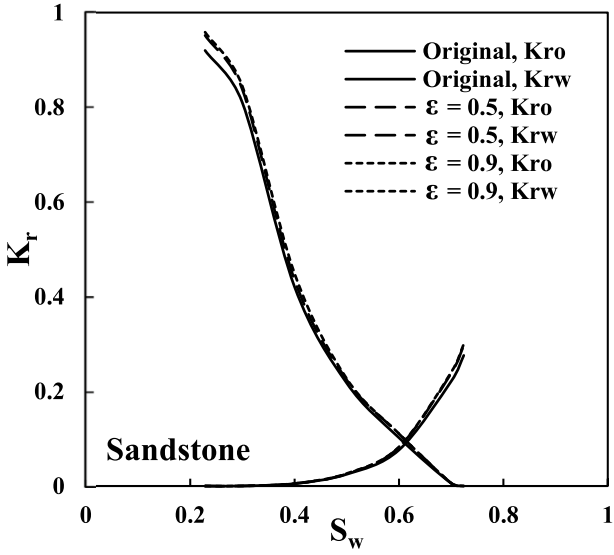

Fig. 9 Water-oil relative permeability curves in the sandstone's original image, and their comparison with those computed with the curvelet-thresholded images

and numerical simulations of two-phase flow are carried out in the curvelet-transformed images, with the numerical results inversed curvelet-transformed back to the real space. To carry out such simulations, one must take the CT of the governing equations. Since digital CTs operate in the frequency domain, one substitutes the Fourier transforms $\hat{f}(\boldsymbol{\omega})$ and $U(R_{\theta_l}\boldsymbol{\omega})$ in Eq. (7). We first rewrite the second-order term of the momentum equation, Eq. (14), as, $\boldsymbol{\nabla}\cdot(\mu\boldsymbol{\nabla}\,\mathbf{v})=\boldsymbol{\nabla}\mu\cdot\boldsymbol{\nabla}\mathbf{v}+\mu\nabla^2\mathbf{v}$. The curvelet transform of the gradient $\boldsymbol{\nabla}F$ of a function F is given by

$$\frac{1}{\cos\theta_l}\frac{\partial\mathcal{F}_{j,l,k}}{\partial y_1}\mathbf{e}_1+\frac{\partial\mathcal{F}_{j,l,k}}{\partial y_2}\mathbf{e}_2, \tag{16}$$

where $\mathcal{F}_{j,l,k}$ is the CCs associated with F, (y_1, y_2) are the coordinates in the curvelet space, and $\mathbf{e}_1$ and $\mathbf{e}_2$ are unit vectors associated with y_1 and y_2. The CT of the Laplacian $\nabla^2 G$ of a function G is given by

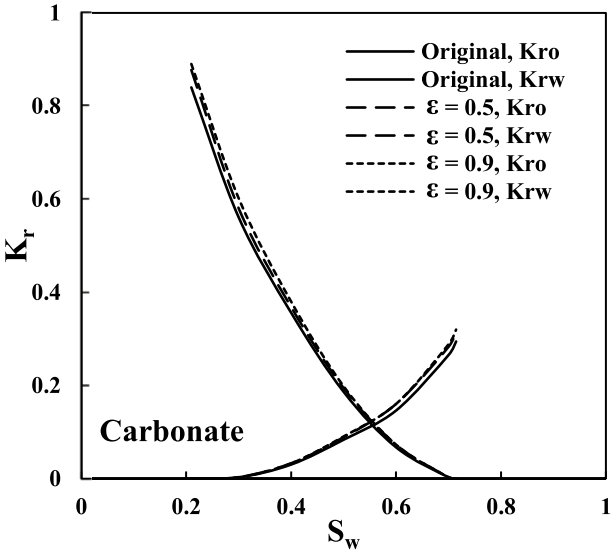

Fig. 10 Same as in Fig. 9, but for the carbonate porous medium

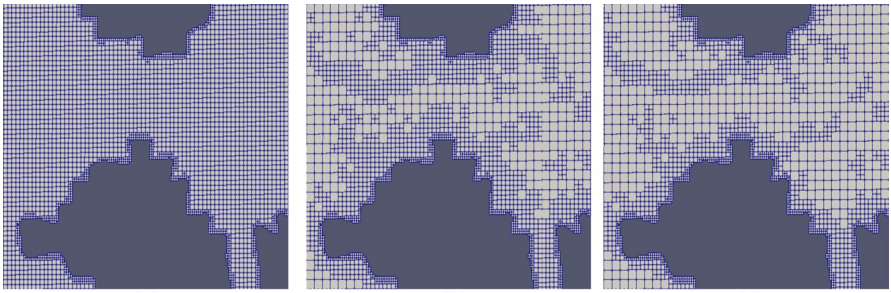

Fig. 11 The structure of the computational grid in a small portion of **a** the original image of the sandstone; **b** the coarsened image with the threshold $\epsilon = 0.5$, and **c** with $\epsilon = 0.9$

Table 1 Comparison of the number of grid blocks N, the computation times, and the oil residual saturation S_{or}, computed with the original and curvelet transform-thresholded images

Sandstone	N	Threshold ϵ	S_{or}	Time (CPU sec)
Original image	859,973		0.276	19,241
Curvelet-transformed image	12,646	0.5	0.286	173
Curvelet-transformed image	8187	0.7	0.288	139
Curvelet-transformed image	6871	0.9	0.289	127
Carbonate				
Original image	879,103		0.288	38,827
Curvelet-transformed image	13,833	0.5	0.291	359
Curvelet-transformed image	9116	0.7	0.296	283
Curvelet-transformed image	7727	0.9	0.298	261

$$(1+\tan^2\theta_l)\frac{\partial^2\mathcal{G}_{j,l,k}}{\partial y_1^2}+\frac{\partial^2\mathcal{G}_{j,l,k}}{\partial y_2^2}-2\tan\theta_l\frac{\partial^2\mathcal{G}_{j,l,k}}{\partial y_1\partial y_2}, \tag{17}$$

with $\mathcal{G}_{j,l,k}$ being the CC associated with G. One then solves the curvelet-transformed governing equation in the curvelet-transformed image by discretizing it and defining the scale j, direction l, and translation parameter $\mathbf{k}=(k_1,k_2)\in Z^2$, with $(y_1,y_2)=(2^{-j}k_1,2^{-j/2}k_2)$. The inverse CT of the numerical solution is then computed.

It has been shown (Aljasmi and Sahimi 2020) that if this procedure is followed, the computations will be speeded up by a factor of four or better, even if the image in the curvelet space is not processed. Clearly, then, if the image is denoised, and the computations are still carried out in the CT of the denoised image, the speed-up factor will be very large, comparable with what is presented in Table 1. The reason for the higher efficiency even without thresholding is that a coarser computational grid suffices in the curvelet space, because many of the CCs of the image are either very small and, thus, do not make significant contributions, or that due to the correlations they are close to those of their neighbors, indicating a relatively smooth local environment, hence allowing use of larger grid blocks. As such noisy pixels may be due to artifacts during image processing, their removal would actually lead to more accurate simulation of flow and transport processes than what would obtain with the original image.

7.3 Simulation in Three-Dimensional Images

Although the CTs were originally developed for 2D images, their extension to 3D systems has also been proposed and developed (Ying et al. 2005; Woiselle et al. 2010). Thus, one may use such 3D CTs in the computations with 3D images. Alternatively, one may divide a 3D image into a large number of 2D slices, apply the methodology described here to each 2D image, and then stack together the curvelet-transformed 2D images to reconstruct a 3D coarser image. Care must be taken to ensure that after curve-transforming and thresholding, the transition from one 2D slice to the next is seamless, and does not generate any artifacts. We are currently carrying out simulations of two-phase flow in 3D images of porous media using the CTs, the results of which will be reported in the near future.

8 Summary

Advances in instrumentations, together with rapid increase in the speed of computations, have made it possible to begin simulation of multiphase flow in 2D and 3D images of heterogeneous porous media, hence avoiding altogether the assumption and approximations that are involved in the development of models of porous media. However, as image-based simulation of multiphase flow in heterogeneous porous media becomes more practical, one must still address the issue of its high computational cost. In this paper, we described a new methodology to address the issue, which is based on curvelet transforming the image and denoising it by removing those details of the image that do not contribute significantly to the simulation. The computations in the less noisy, and hence more coarsened images, yield results that are as accurate as those in the original ones, but with a speedup factor of 100–150 or higher. Thus, the methodology represents a significant step toward achieving the ultimate goal of such simulations, namely, making image-based simulation of multiphase flow in heterogeneous porous media a standard practice.

Acknowledgements A.A. is grateful to the Public Authority for Applied Education and Training of Kuwait for a Ph.D. scholarship. This work was also supported in part by the National Science Foundation.

References

Aljasmi, A., Sahimi, M.: Efficient image-based simulation of flow and transport in heterogeneous porous Media: Application of curvelet transforms. Geophys. Res. Lett. **47**, e2019GL085671 (2020)
Al-Zubi, S., Islam, N., Abbod, M.: Multiresolution analysis using wavelet, ridgelet, and curvelet transforms for medical image segmentation. Int. J. Biomed. Imaging **2011**, 136034 (2011)
Arns, C.H., Knackstedt, M.A., Pinczewski, W.V., Garboczi, E.: Computation of linear elastic properties from microtomographic images: methodology and agreement between theory and experiment. Geophysics **67**, 1348 (2002)
Arns, C.H., Knackstedt, M.A., Pinczewski, W.V., Lindquist, W.B.: Accurate computation of transport properties from microtomographic images. Geophys. Res. Lett. **28**, 3361 (2001)
Aslannejad, H., Hassanizadeh, S.M.: Study of hydraulic properties of uncoated paper: image analysis and pore-scale modeling. Transp. Porous Media **120**, 67 (2017)
Aslannejad, H., Hassanizadeh, S.M., Celia, M.A.: Characterization of the interface between coating and fibrous layers of paper. Transp. Porous Media **127**, 143 (2019)
Babaei, M., King, P.R.: A comparison between wavelet and renormalization upscaling methods and iterative upscaling-downscaling scheme. SPE Reservoir Simul. Symp. **1**, 469 (2011)
Bakhshian, S., Shi, Z., Sahimi, M., Tsotsis, T.T., Jessen, K.: Image-based modeling of gas adsorption and swelling in high-pressure porous formations. Sci. Rep. **8**, 8249 (2018)
Bear, J.: Dynamics of Fluids in Porous Media. Dover, Mineola (1972)
Berg, S., Ott, H., Klapp, S.A., Schwing, A., Neiteler, R., Brussee, N., Makurat, A., Leu, L., Enzmann, F., Schwarz, J.-O., Kersten, M., Irvine, S., Stampanoni, M.: Real-time 3D imaging of Haines jumps in porous media flow. Proc. Natl. Acad. Sci. USA **110**, 3755 (2013)
Blunt, M.J.: Effects of heterogeneity and wetting on relative permeability using pore level modeling. SPE J. **2**, 70 (1997)
Blunt, M.J.: Multiphase Flow in Permeable Media: A Pore-Scale Perspective. Cambridge University Press, Cambridge (2017)
Blunt, M.J., King, M.J., Scher, H.: Simulation and theory of two-phase flow in porous media. Phys. Rev. A **46**, 7680 (1992)
Blunt, M.J., King, P.R.: Relative permeabilities from two- and three-dimensional pore-scale network modelling. Transp. Porous Media **6**, 407 (1991)
Blunt, M.J., Scher, H.: Pore-level modeling of wetting. Phys. Rev. E **52**, 6387 (1995)
Candés, E., Demanent, L., Donoho, D.L., Ying, L.: Fast discrete curvelet transforms. Multiscale Model. Simul. **5**, 861 (2005)
Chandler, R., Koplik, J., Lerman, K., Willemsen, J.: Capillary displacement and percolation in porous media. J. Fluid Mech. **119**, 249 (1982)
Dashtian, H., Sahimi, M.: Coherence index and curvelet transformation for denoising geophysical data. Phys. Rev. E **90**, 042810 (2014)
Daubechies, I.: Orthonormal basis of compactly supported wavelets. Commun. Pure Appl. Math. **41**, 901 (1988)
Daubechies, I.: Ten Lecture on Wavelets. SIAM, Philadelphia (1992)
Donoho, D.L.: Wedgelets: nearly minimax estimation of edges. Ann. Statist. **27**, 859 (1999)
Ebrahimi, F.: Invasion percolation: A computational algorithm for complex phenomena. Comput. Sci. Eng. **12**(2), 84 (2010)
Ebrahimi, F., Sahimi, M.: Multiresolution wavelet coarsening and analysis of transport in heterogeneous porous media. Phys. A **316**, 160 (2002)
Ebrahimi, F., Sahimi, M.: Multiresolution wavelet scale up of unstable miscible displacements in flow through porous media. Transp. Porous Media **57**, 75 (2004)
Francois, M.M., Cummins, S.J., Dendy, E.D., Kothe, D.B., Sicilian, J.M., Williams, M.M.: A balanced-force algorithm for continuous and sharp interfacial surface tension models within a volume tracking framework. J. Comput. Phys. **213**, 141 (2006)
Friedlingstein, P., Solomon, S.: Contributions of past and present human generations to committed warming caused by carbon dioxide. Proc. Natl. Acad. Sci. USA **102**, 10832 (2005)
Ghanbarian, B., Sahimi, M., Daigle, H.: Modeling relative permeability of water in soil: Application of effective-medium approximation and percolation theory. Water Resour. Res. **52**, 5025 (2016)

Ghassemzadeh, J., Hashemi, M., Sartor, L., Sahimi, M.: Pore network simulation of fluid imbibition into paper during coating processes: I. Model development. AIChE J. **47**, 519 (2001)
Ghassemzadeh, J., Sahimi, M.: Pore network simulation of fluid imbibition into paper during coating III: Modeling of the two-phase flow. Chem. Eng. Sci. **59**, 2281 (2004)
Gueyffier, D., Li, J., Nadim, A., Scardovelli, R., Zaleski, S.: Volume-of-fluid interface tracking with smoothed surface stress methods for three-dimensional flows. J. Comput. Phys. **152**, 423 (1999)
Heiba, A.A., Sahimi, M., Scriven, L.E., Davis, H.T.: Percolation theory of two-phase relative permeability. SPE Reservoir Eng. **7**, 123 (1992)
Helmig, R., Schulz, P.: Multiphase Flow and Transport Processes in the Subsurface. Springer, Berlin (1997)
Herrmann, F.J., Wang, D., Hennenfent, G., Moghaddam, P.P.: Curvelet-based seismic data processing: A multiscale and nonlinear approach. Geophysics **73**, A1 (2007)
Hunt, A.G., Sahimi, M.: Flow, transport, and reaction in porous media: Percolation scaling, critical-path analysis, and Effective-Medium Approximation. Rev. Geophys. **55**, 993 (2017)
Iglauer, S., Favretto, S., Spinelli, G., Schena, G., Blunt, M.J.: X-ray tomography measurements of power-law cluster size distributions for the nonwetting phase in sandstones. Phys. Rev. E. **82**, 056315 (2010)
Kantzas, A., Chatzis, I.: Network simulation of relative permeability curves using a bond correlated-site percolation model of pore structure. Chem. Eng. Commun. **69**, 191 (1988)
Knackstedt, M.A., Sheppard, A.P., Sahimi, M.: Pore network modeling of two-phase flow in porous rock: The effect of correlated heterogeneity. Adv. Water Resour. **24**, 257 (2001)
Kohanpur, A.H., Rahromostaqim, M., Valocchi, A.J., Sahimi, M.: Two-phase flow of CO_2-brine in a heterogeneous sandstone: characterization of the rock and comparison of the lattice-Boltzmann, pore-network, and direct numerical simulation methods. Adv. Water Resour. **135**, 103439 (2020)
Larson, R.G., Scriven, L.E., Davis, H.T.: Percolation theory of residual phases in porous media. Nature **268**, 409 (1977)
Lemmens, H.J., Butcher, R., Botha, P.W.S.K.: FIB/SEM and SEM/EDX: a new dawn for the SEM in the core lab? Petrophysics **52**, 452 (2011)
Ma, J., Plonka, G.: Computing with curvelets: From image processing to turbulent flows. Comput. Sci. Eng. **11**(2), 72 (2009)
Mallat, S.G.: A theory for multiresolution signal decomposition: the wavelet representation. IEEE Trans. Pattern Recog. Machine Intell. **11**, 674 (1989)
Mallat, S.G.: Multiresolution approximations and wavelet orthonormal bases of $L^2(R)$. Trans. Am. Math. Soc. **315**, 69 (1989)
Mehrabi, A.R., Sahimi, M.: Coarsening of heterogeneous media: application of wavelets. Phys. Rev. Lett. **79**, 4385 (1997)
Neelamani, R., Baumstein, A.I., Gillard, D.G., Hadidi, M.T., Soroka, W.L.: Coherent and random noise attenuation using the curvelet transform. The Leading Edge **27**, 129 (2008)
Nordbotten, J.M., Celia, M.A.: Geological Storage of CO_2: Modeling Approaches for Large-Scale Simulation. Wiley, New York (2011)
Oak, M., Baker, L., Thomas, D.: Three-phase relative permeability of Berea sandstone. J. Pet. Technol. **42**, 1054 (1990)
Olhede, S., Walden, A.T.: The Hilbert spectrum via wavelet projections. Proc. R. Soc. Lond. A **460**, 955 (2004)
Pancaldi, V., Christensen, K., King, P.R.: Permeability up-scaling using Haar wavelets. Transp. Porous Media **67**, 395 (2007)
Piri, M., Blunt, M.J.: Three-dimensional mixed-wet random pore-scale network modeling of two- and three-phase flow in porous media. I. Model description. Phys. Rev. E **71**, 026301 (2005)
Piri, M., Blunt, M.J.: Three-dimensional mixed-wet random pore-scale network modeling of two- and three-phase flow in porous media. II. Results. Phys. Rev. E **71**, 026302 (2005)
Porter, M.L., Wildenschild, D., Grant, G., Gerhard, J.I.: Measurement and prediction of the relationship between capillary pressure, saturation, and interfacial area in a NAPL-water-glass bead system. Water Resour. Res. **46**, W08512 (2010)
Raeini, A.Q.: *Modelling Multiphase Flow Through Micro-CT Images of the Pore Space*, Ph.D. Thesis, Imperial College of London (2013)
Raeini, A.Q., Blunt, M.J., Bijeljic, B.: Modelling two-phase flow in porous media at the pore scale using the volume-of-fluid method. J. Comput. Phys. **231**, 5653 (2012)
Raeini, A.Q., Blunt, M.J., Bijeljic, B.: Direct simulations of two-phase flow on micro-CT images of porous media and upscaling of pore-scale forces. Adv. Water Resour. **74**, 116 (2014)
Rasaei, M.R., Sahimi, M.: Upscaling and simulation of waterflooding in heterogeneous reservoirs using wavelet transformations: Application to the SPE-10 model. Transp. Porous Media **72**, 311 (2008)

Rasaei, M.R., Sahimi, M.: Upscaling of the permeability by multiscale wavelet transformations and simulation of multiphase flows in heterogeneous porous media. Comput. Geosci. **13**, 187 (2009)
Rezapour, A., Ortega, A., Sahimi, M.: Upscaling of geological models of oil reservoirs with unstructured grids using lifting-based graph wavelet transforms. Transp. Porous Media **127**, 661 (2019)
Sahimi, M.: Flow and Transport in Porous Media and Fractured Rock, 2nd edn. Wiley, Weinheim (2011)
Sahimi, M., Heiba, A.A., Davis, H.T., Scriven, L.E.: Dispersion in flow through porous media: II. Two-phase flow. Chem. Eng. Sci. **41**, 2123 (1986)
Sankey, M.H., Holland, D.J., Sederman, A.J., Gladden, L.F.: Magnetic resonance velocity imaging of liquid and gas two-phase flow in packed beds. J. Magn. Reson. **196**, 142 (2009)
Sheppard, S., Mantle, M.D., Sederman, A.J., Johns, M.L., Gladden, L.F.: Magnetic resonance imaging study of complex fluid flow in porous media: flow patterns and quantitative saturation profiling of amphiphilic fracturing fluid displacement in sandstone cores. Magn. Reson. Imaging. **21**, 365 (2003)
Shokri, N.: Pore-scale dynamics of salt transport and distribution in drying porous media. Phys. Fluids **26**, 012106 (2014)
Shokri, N., Lehmann, P., Or, D.: Characteristics of evaporation from partially-wettable porous media. Water Resour. Res. **45**, W02415 (2009)
Shokri, N., Lehmann, P., Or, D.: Liquid phase continuity and solute concentration dynamics during evaporation from porous media—pore scale processes near vaporization surface. Phys. Rev. E **81**, 046308 (2010)
Shokri, N., Sahimi, M., Or, D.: Morphology, propagation dynamics and scaling characteristics of drying fronts in porous media. Geophys. Res. Lett. **39**, L09401 (2012)
Shokri-Kuehni, S.M.S., Vetter, T., Webb, C., Shokri, N.: New insights into saline water evaporation from porous media: complex interaction between evaporation rates, precipitation and surface temperature. Geophys. Res. Lett. **44**, 5504 (2017)
Shokri-Kuehni, S.M.S., Norouzirad, M., Webb, C., Shokri, N.: Impact of type of salt and ambient conditions on saline water evaporation from porous media. Adv. Water Resour. **105**, 154 (2017)
Shokri-Kuehni, S.M.S., Bergstad, M., Sahimi, M., Webb, C., Shokri, N.: Iodine k-edge dual energy imaging reveals the influence of particle size distribution on solute transport in drying porous media. Sci. Rep. **10**, 10731 (2018)
Starck, J.-L., Candés, E.J., Donoho, D.L.: The curvelet transform for image denoising. IEEE Trans. Image Process. **11**(6), 670 (2002)
Swerin, A.: Dimensional scaling of aqueous ink imbibition and inkjet printability on porous pigment coated paper A revisit. Ind. Eng. Chem. Res. **57**, 49 (2018)
Tahmasebi, P., Sahimi, M., Kohanpur, A.H., Valocchi, A.J.: Pore-scale simulation of flow of CO_2 and brine in reconstructed and actual 3D rock cores. J. Pet. Sci. Eng. **155**, 21 (2017)
Ubink, O.: *Numerical Prediction of Two Fluid Systems with Sharp Interfaces*, Ph.D. Thesis, Imperial College of London (1997)
Wildenschild, D., Armstrong, R.T., Herring, A.L., Young, I., Young, I.M., Carey, J.W.: Exploring capillary trapping efficiency as a function of interfacial tension, viscosity, and flow rate. Energy Procedia **4**, 4945 (2014)
Wilkinson, D., Willimsen, J.F.: Invasion percolation: a new form of percolation theory. J. Phys. A **16**, 3365 (1983)
Woiselle, A., Starck, J.-L., Fadili, J.: 3D curvelet transforms and astronomical data restoration. Appl. Comput. Harmonic **28**, 171 (2010)
Ying, L., Demanet, L., Candés, E.: 3D discrete curvelet transform. *Proceedings of SPIE5914, Wavelets XI, 591413* (2005)